Shape coexistence effects and superdeformation in ^{84}Zr

J. Dudek
Science and Engineering Research Council Daresbury Laboratory, Warrington WA4 4AD, United Kingdom and Centre de Recherches Nucléaires, F-67037 Strasbourg Cedex, France

W. Nazarewicz*
The Niels Bohr Institute, DK-2100 Copenhagen, Denmark and Department of Mathematical Physics, Lund Institute of Technology, S-22110 Lund, Sweden

N. Rowley
Science and Engineering Research Council Daresbury Laboratory, Warrington WA4 4AD, United Kingdom
(Received 24 November 1986)

The high-spin spectrum of ^{84}Zr is studied using the Strutinsky-Bogolyubov cranking model with a Woods-Saxon average potential. Calculations explain observed irregularities in the ^{84}Zr yrast line in terms of band crossings involving aligned $g_{9/2}$ proton and neutron bands. A transition to the superdeformed shape is predicted to occur around $I \sim 30\hbar$. Experimental data are consistent with the nucleus having a well deformed ($\beta_2 \simeq 0.3$) and triaxial ($\gamma \simeq -20°$) shape.

I. INTRODUCTION

During the last decade, high-spin studies have focused mainly on rare earth nuclei. Using the methods of discrete γ-ray spectroscopy, states above $I = 40\hbar$ were observed directly in some nuclei (see, e.g., Refs. 1 and 2), while quasicontinuum studies have given indirect information about the highest spin range up to $I = (50–60)\hbar$. (Very recently, a superdeformed band extending up to $60\hbar$ has also been observed in ^{152}Dy by discrete spectroscopy, Ref. 3.) The relatively light nuclei with $Z \simeq 36$ and $N \simeq 40$ have also been studied, showing interesting structural features. Although the term "high spin" traditionally already applies in these light nuclei at $I \simeq 16\hbar$, it was the shape coexistence effects observed at low spins in light ^{32}Ge, ^{34}Se, and ^{36}Kr isotopes with $N \simeq 38$ that attracted particular attention here (see, e.g., Ref. 4 and references quoted therein). Only relatively recently have heavy ion fusion evaporation reaction studies revealed various phenomena of these nuclei at $I \geq 16\hbar$ (Refs. 5–9), i.e., at rotational frequencies $\omega \geq 700$ keV/$\hbar$. For $^{84}_{40}Zr_{44}$, states with spin as high as $I^{\pi} = (36^{+})$ have been reported,[5] and despite the fact that the experimental results are uncertain for $I \geq 20\hbar$, they indicate the possibility of observing very high multiplicity events in nuclei in the $A \simeq 80$ mass range.

Although the microscopic effects ruling the high-spin behavior of both groups of nuclei are principally the same (single-particle alignment, pairing variation due to rotation, shape coexistence resulting from the shell structure), in the light nuclei they combine to form an altogether different mechanism, leading to very strong shape effects. The underlying single-particle level structure is dominated by a particularly high abundance of large energy gaps corresponding to oblate shapes at Z and $N = 34$ and 36, to spherical shape at Z and $N = 40$, and to various prolate deformations ranging from $\beta_2 = 0.20$ up to $\beta_2 = 0.50–0.70$ for Z and $N = 34$, 38, 40, 42, and 44 (cf. Fig. 1 of Ref. 10). The large quadrupole moments and moments of inertia observed recently in a number of Br, Kr, Rb, and Sr isotopes[5–9] can be explained theoretically[10,11] in terms of large ($\beta_2 \simeq 0.40$) ground state equilibrium deformations in these nuclei.

Recent measurements of very high spin states in the ^{84}Zr nucleus make it possible to test detailed theoretical calculations concerning its high-spin behavior and aiming at the study of the different competing mechanisms. The analysis presented here applies powerful phenomenological techniques developed in the past (cranking model, Strutinsky renormalization, the Hartree-Fock-Bogolyubov method; for details, see Ref. 12 and references therein) incorporated consistently into one treatment. Such an approach allows for studying simultaneously the deformation, single-particle alignment, and the pairing effects together with their possible competition and interplay.

In the following the general features of the calculations are described and the results are discussed in detail.

II. THE MODEL

The microscopic, quantum mechanical basis of interplay between deformation, single-particle alignment, and pairing effects can often be understood from the underlying single-particle structure. Calculations[13] employing the deformed Nilsson potential predicted small oblate ($\gamma = 60°$) deformations for ^{84}Zr in the spin range $(10–40)\hbar$, contradicting experimental data[5] which show rather regular collective bands connected via enhanced $\beta(E2)$ transitions in this nucleus. In the present study we apply the Woods-Saxon Strutinsky-Bogolyubov cranking model applied previously[10] in the study of low and high spin properties of selected $A \sim 80$ nuclei. In particular, it has been shown there that the model gives a correct description of both single-particle level order and overall

rotational behavior in the mass region discussed. In the following the definition of the applied Woods-Saxon model is given, followed by remarks on the treatment of rotation and pairing.

A. The single-particle potential

The single-particle levels are generated by the deformation-dependent Woods-Saxon potential

$$V(\mathbf{r},\beta)=\frac{V_0}{1+\exp[\mathrm{dist}(\mathbf{r};\beta)/a]}\ , \tag{1}$$

where the function $\mathrm{dist}(\mathbf{r},\beta)$ denotes the distance of a point $\mathbf{r}$ from the nuclear surface Σ parametrized in terms of the quadrupole and hexadecapole degrees of freedom. The shape parametrization used includes nonaxial deformations:

$$\Sigma:\ R(\theta,\phi)=r_0A^{1/3}C(\beta)\left[1+\sum_{\mu=0,\pm2}\alpha_{2\mu}Y^*_{2\mu}(\theta,\phi)+\sum_{\mu=0,\pm2,\pm4}\alpha_{4\mu}Y^*_{4\mu}(\theta,\phi)\right]\ , \tag{2}$$

and

$$\beta\equiv(\alpha_{20},\alpha_{2+2},\alpha_{2-2},\alpha_{40},\alpha_{4-2},\alpha_{4+2},\alpha_{44},\alpha_{4-4})$$

denotes the set of all the shape deformation parameters. In Eq. (2), $C(\beta)$ is calculated at each deformation separately in order to fulfill the constant volume condition. The quantity $R(\theta,\phi)$ is the distance of any point on the nuclear surface (direction specified by the polar angles θ and ϕ) from the origin of the coordinate system.

After assuming that the shape parametrization preserves three symmetry planes and requesting the hexadecapole degrees of freedom to be functions of the scalars in the quadrupole tensor $\alpha_{2\mu}$ (see Ref. 14), we reduce[10] the number of independent coefficients to three: β_2, γ, and β_4, where

$$\alpha_{20}=\beta_2\cos\gamma\ , \tag{3a}$$

$$\alpha_{22}=\alpha_{2-2}=-\frac{1}{\sqrt{2}}\beta_2\sin\gamma\ , \tag{3b}$$

$$\alpha_{40}=\tfrac{1}{6}\beta_4(5\cos^2\gamma+1)\ , \tag{3c}$$

$$\alpha_{42}=\alpha_{4-2}=-\tfrac{1}{12}\sqrt{30}\beta_4\sin^2\gamma\ , \tag{3d}$$

$$\alpha_{44}=\alpha_{4-4}=\tfrac{1}{12}\sqrt{70}\beta_4\sin^2\gamma\ . \tag{3e}$$

This choice of parametrization guarantees that at each multiple of $\gamma=60°$ we return to axially symmetric shapes irrespective of the value of β_4. The original richness of hexadecapole shapes [cf. Eq. (2)] is obviously diminished in favor of decreased computational effort. At axially symmetric shapes, β_4 has exactly the same meaning as in all the standard shape parametrizations.

The spin-orbit potential is defined as usual as a scalar composed of grad, $\mathbf{p}$, and $\mathbf{s}$:

$$V_{\mathrm{so}}(\mathbf{r},\beta)=-\lambda\left[\frac{\hbar}{2mc}\right]^2[\mathrm{grad}V(\mathbf{r},\beta)\times\mathbf{p}]\cdot\mathbf{s}\ , \tag{4}$$

where λ denotes the strength parameter of the effective spin-orbit force acting on the individual nucleons.. In fact, the radius parameter of the spin-orbit potential should, in general, be different from that of the corresponding central part (see, e.g., Ref. 15); this is equivalent to having introduced a new surface Σ_{so} differing from the one in Eq. (2) by the numerical value of the constant r_0. In the present paper we use the *universal Woods-Saxon parameters* of Ref. 16, which give a good description of the single-particle states, at least in nuclei with $A\geq40$ (see, e.g., discussion in Ref. 17).

Our definition of the deformed potential is a straightforward generalization of the spherical Woods-Saxon potential:

$$V(r)=\frac{V_0}{1+\exp[(r-R_0)/a]}\ , \tag{5}$$

in which the distance from the nuclear surface $(r-R_0)$ is replaced by the function $\mathrm{dist}(\mathbf{r},\beta)$. Therefore the generalization of Eq. (5) automatically preserves the condition of a constant surface thickness of the nuclear shape, independent of the point on the surface. Any parametrization which does not involve an exactly linear functional of the distance in the exponent in Eq. (1) is called here *Woods-Saxon-like*. The Woods-Saxon-like potentials contain differences when compared with the potential represented in Eqs. (1,4) which, in general, grow with increasing deformation, causing systematic differences in the single-particle spectra even if the same values of the potential parameters are used in the Woods-Saxon and Woods-Saxon-like approaches.

The Schrödinger equation with the single-particle Woods-Saxon Hamiltonian

$$H_{\mathrm{WS}}=T+V(\mathbf{r};\beta)+V_{\mathrm{so}}(\mathbf{r};\beta)+\tfrac{1}{2}(1+\tau_3)V_{\mathrm{Coul}}(\mathbf{r};\beta)\ , \tag{6}$$

where the Coulomb potential $V_{\mathrm{Coul}}(\mathbf{r},\beta)$ is added for protons, is solved numerically[18] using the diagonalization method. We used at least $N=14$ deformed harmonic oscillator shells as the single-particle basis; with such a basis cutoff the results are sufficiently stable with respect to a possible enlargement of the basis.

B. Rotation

In order to take into account the effect of rotation, we apply the standard cranking approximation. This is equivalent to solving the eigenvalue problem:

$$H^{\omega}\psi^{\omega}_{\nu}=e^{\omega}_{\nu}\psi^{\omega}_{\nu}\ , \tag{7}$$

where, according to the notation in Eq. (6),

$$H^{\omega}\equiv H_{\mathrm{WS}}-\omega j_x\ . \tag{8}$$

In Eqs. (7) and (8), ω is the cranking frequency about the x axis and j_x is the associated component of the angular momentum operator.

The (β_2,γ,β_4) parametrization has all the symmetry properties of Bohr's (β_2,γ) parametrization.[19] In particular, at $\omega=0$ the whole (β_2,γ) plane splits into six equivalent sectors defined by the axes $\gamma=k\pi/3$ (with $k=0,1,\ldots,5$). The cranking model equations (7) and

(8) with $\omega \neq 0$ generally break this symmetry. Then one has to perform the calculations in a full half-plane. The half-plane symmetry applies to any dynamical quantity, particularly the single-particle routhians e_ν^ω of Eq. (7) and all the derived energies, including the Strutinsky-type energies.

The knowledge of the number and location of the total energy minima is a prerequisite for the shape coexistence analysis. In order to obtain the total energy surfaces, we use the Strutinsky method[20] generalized[21,22] to the case of rotation.

However, here we explicitly employ the symmetries of our cranking Hamiltonian, the parity π, and the signature r, and apply the Strutinsky formula separately[23] to different configurations characterized by the set of quantum numbers:

$$\{N_{\tau,\pi,r}, N_{\text{exc}}\} , \tag{9}$$

where $\tau = \text{n,p}$ and $N_{\tau,\pi,r}$ denotes the number of particles of type τ occupying orbitals of parity π and signature r. The quantum number N_{exc} ($N_{\text{exc}} = 1,2,\ldots$) labels the states which differ structurally, although having identical quantum numbers $N_{\tau,\pi,r}$. Such an approach[23,24] enables us to study the lowest energy bands of various configurations, their crossings, shape evolution, etc.

In order to compare the theoretical predictions with the experimental data, however, the pairing must be taken into account since they dominate the excitation pattern, especially at low spin. We use the simple monopole pairing force, i.e., we replace

$$H_{\text{WS}} \rightarrow H_{\text{WS}} - \sum_{\tau=\text{n,p}} G^{(\tau)} \sum_{\nu\nu'} C_\nu^\dagger C_{\bar{\nu}}^\dagger C_{\bar{\nu}} C_{\nu'} , \tag{10}$$

where the $G^{(\text{n})}$ and $G^{(\text{p})}$ are the average matrix elements of the pairing interaction. In our paper we used values of $G^{(\tau)}$ from Ref. 10. In the presence of pairing the cranking equations (7) and (8) can be solved using the Hartree-Fock-Bogolyubov cranking (HFBC) (also called independent quasiparticle) method[25] (for a detailed description of this method, see, e.g., Ref. 12). The HFBC method allows one to calculate approximately the total energy of the system and the total angular momentum as functions of the rotational frequency ω, from which quantities such as the kinematic and dynamical moments of inertia, the aligned angular momenta, etc. can also be derived.

In the following sections we apply the Woods-Saxon model described above to the case of ^{84}Zr nucleus.

III. SHAPE EVOLUTION IN ^{84}Zr

A. Ground-state shapes of neutron deficient even-even Zr isotopes

The equilibrium deformation of the zirconium isotopes result from the interplay between the spherical Z and $N = 40$ gaps and the prolate Z and $N = 38$, 40, 42, and 44 gaps in the single-particle spectrum. Figure 1 shows the calculated potential energy surfaces (PES's) at $I = 0$ (with the inclusion of pairing) for the sequence of neutron deficient Zr isotopes. In the isotopes with $N \leq 42$ the ground state corresponds to a strongly elongated shape with $\beta_2 \simeq 0.38$, $\gamma = 0°$. The spherical Z and $N = 40$ gap manifests itself by the presence of local spherical minima for ^{80}Zr and ^{82}Zr. In the nucleus $^{80}_{40}Zr_{40}$, which has sometimes been assumed to be a quasimagic system, the spherical minimum is predicted to lie about 1.7 MeV above the deformed ground state. This is consistent with the very recently obtained[26] results on this nucleus, which indicate a ground-state deformation $\beta_2 \simeq 0.42$, and is further supported by the new deformed shell structure systematic in

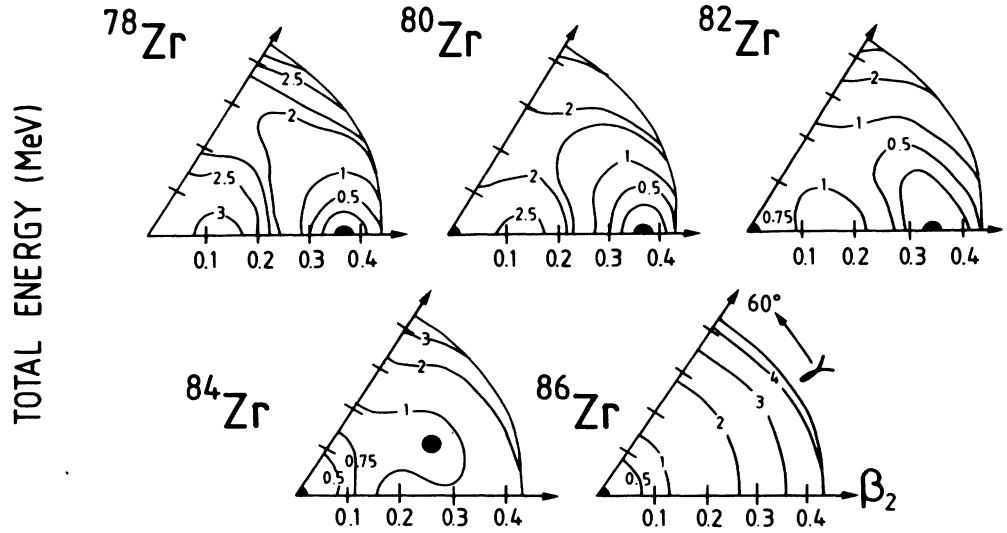

FIG. 1. Total energy surfaces in the (β_2,γ) plane for the doubly even neutron deficient Zr isotopes. Results are obtained using the Woods-Saxon potential and the BCS pairing model. At each (β_2,γ) deformation we used the hexadecapole deformation, which minimized the liquid drop energy. The energy (in MeV) is given relative to the absolute minimum. The black dots show the location of the energy minima.

terms of pseudo-SU_3 symmetry; see Ref. 27. Due to the large quadrupole equilibrium deformations, collective rotational spectra are predicted to dominate the excitation pattern of $^{78-82}$Zr nuclei.

In the heavier nuclei with $N \geq 44$, the spherical structures determined by the presence of $Z=40$ and $N=50$ gaps dominate. In the ground-state PES of ^{84}Zr there are two local minima, i.e., one at $\beta_2=0$ and one at $\beta_2=0.28$, $\gamma \simeq 20°$. The spherical one lies about 800 keV below the triaxial minimum. The states corresponding to the two minimum are expected to interact with each other, leading to a mixed spherical-triaxial ground-state configuration, as in the light Ge and Se nuclei. The deformed structure is not present in ^{86}Zr, which possesses only one spherical minimum. The reduction of the quadrupole deformation in ^{84}Zr is reflected by the small value of the experimental quadrupole moment $|Q_2| \simeq 1.8\ e$ b, Ref. 5, which is almost one-half of the corresponding value for ^{78}Sr, Ref. 28, one of the best deformed nuclei in the $A \simeq 80$ mass region.

B. Interplay between weakly and strongly deformed structures in ^{84}Zr

In order to get some idea about the deformation changes which may occur in the yrast lines in ^{84}Zr, we first calculated PES's for a number of low-lying configurations without considering pairing correlations. It has been argued previously[10,29] that the equilibrium deformation obtained from the solution of the unpaired problem gives a reasonable estimate of deformations computed including pairing correlations.

It has proved very useful to represent the PES's at different spin values in the form of maps employing a portion of the (β_2,γ) plane. However, if one takes into account the number of configurations which become yrast at some spin value and tries to follow the rotational evolution of shapes associated with those configurations, the number of maps necessary for such an illustration becomes impractically large. In order to illustrate the shape evolution in ^{84}Zr, we thus limited ourselves to the case of the PES's corresponding to total parity

$$\pi_{\rm tot}=\pi_\pi\pi_\nu=+1$$

and total signature

$$r_{\rm tot}=r_\pi r_\nu=+1\ .$$

In such a case the PES's are composed of several pieces, corresponding to various configurations specified in terms of $(N_{\tau,\pi,r},N_{\rm exc}=1)$, but with the following constraint: $\pi_{\rm tot}=r_{\rm tot}=1$. The notation $N_{\rm exc}=1$ signifies that all these pieces correspond to yrast energies in the respective deformation regions.

An example of such calculations is given in Fig. 2 for

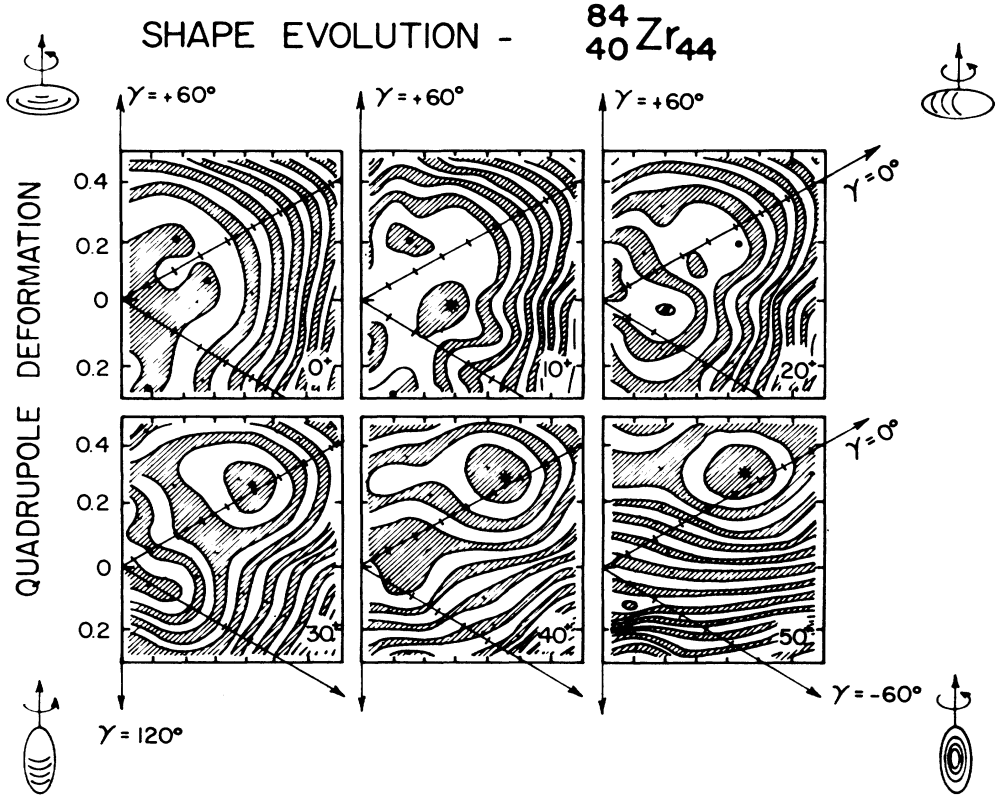

FIG. 2. Total energy surfaces for ^{84}Zr at $I^\pi=0^+,10^+,\ldots,50^+$. Pairing is included only at $I^\pi=0$. The distance between the contour lines is 1 MeV. The position of the absolute minimum is indicated by an asterisk, while the positions of the secondary minima are indicated with dots.

six spin values ($I=0\hbar, 10\hbar, \ldots, 50\hbar$). The polar (β_2,γ) coordinate system is indicated by four axes corresponding, in clockwise order, to $\gamma=60°, 0°, -60°$, and $-120°$. The $\gamma=60°$ axis corresponds to noncollective rotation of an oblate shape.

For $I^\pi=0^+$, there are four local minima, i.e., at $\beta_2=0$ and $\beta_2=0.28$ ($\gamma=+20°$, $-20°$, and $-100°$). The presence of the minima at $\gamma=-20°$ and $100°$ results from the symmetry of Bohr's shape parametrization; these are merely reflections of the minimum at $\gamma=+20°$ (cf. Fig. 1 and discussion in Sec. II B). Such a landscape at $I=0$ implies that for $I\neq 0$ there are, in fact, four different possibilities of accommodating the angular momentum in the system. They are by a collective rotation with triaxial shapes at $\gamma=+20°$, $-20°$, and $-100°$, and by a particle-hole (noncollective) excitation mechanism at the spherical shape, $\beta_2\simeq 0$.

The results presented in Fig. 2 show, however, that collective rotation at $\beta_2\simeq 0.28$ and $\gamma\simeq -(20°-30°)$ quickly becomes energetically most favorable. For $I=10\hbar$ the triaxial minima at $\gamma\simeq +30°$ and $-100°$ lie about 700 keV above the minimum with $\gamma\simeq -30°$, and the minimum at spherical shape lies even higher (at about 1.5 MeV).

For $I=20\hbar$ the minimum at almost spherical shape ($\beta_2\simeq 0.08$, $\gamma=60°$) becomes lowest in energy. It corresponds to the so called doubly optimal configuration $\pi(g_{9/2})^2_8\otimes\nu(g_{9/2})^2_8$. A superdeformed minimum ($\beta_2\simeq 0.5$) develops already at $I\simeq 20\hbar$. For $I\sim 30\hbar$ the absolute minimum corresponds to spherical shape, and collective rotation at $\gamma\simeq=-30°$ disappears. At this spin one finds also a superdeformed minimum which eventually becomes yrast at $I=36\hbar$ (see Fig. 3 below). Finally, for $I=40\hbar$ and $50\hbar$, the yrast configuration corresponds to the nearly axial, superdeformed shape with $\beta_2=0.58$, $\gamma\simeq 7°$. This is a qualitative picture of the rotational effects which one should expect to develop in ^{84}Zr with increasing spin.

We shall now investigate in detail the high-spin behavior of the low-lying collective configurations. Rotational bands can be divided into four principal groups, i.e.,

(1) $\pi_{\rm tot}=+$, $r_{\rm tot}=+1$ $(I^\pi=0^+,2^+,4^+,\ldots)$,

(2) $\pi_{\rm tot}=+$, $r_{\rm tot}=-1$ $(I^\pi=1^+,3^+,5^+,\ldots)$,

(3) $\pi_{\rm tot}=-$, $r_{\rm tot}=+1$ $(I^\pi=0^-,2^-,4^-,\ldots)$,

(4) $\pi_{\rm tot}=-$, $r_{\rm tot}=-1$ $(I^\pi=1^-,3^-,5^-,\ldots)$.

All bands within a given (π,r) family can be further distinguished using the occupation quantum numbers (9).

The lowest collective bands in ^{84}Zr, corresponding to all combinations of parity and signature, are presented in Fig. 3. The energies are displayed relative to a parabola ($0.0173I^2$ MeV) in order not to expand the ordinate axis too much. Shape evolution within the discussed bands is shown in Fig. 4. All the bands in Figs. 3 and 4 can be grouped into two sets: the triaxial bands originating from the symmetric minima at ($\beta_2\simeq 0.28$, $\gamma\simeq\pm 20°$) (indicated in Fig. 4 by encircled black dots) and the superdeformed bands with $0.4\leq\beta_2\leq 0.6$. These two sets are discussed separately in the next two subsections.

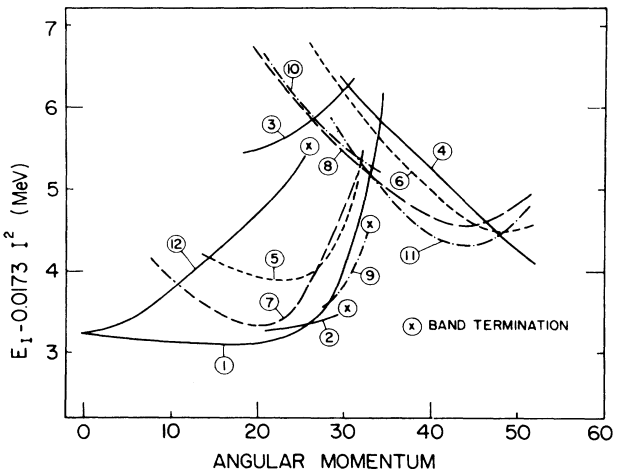

FIG. 3. Low-lying collective rotational bands of both signatures and parities in ^{84}Zr. The energies E_I are displayed relative to an average reference ($0.0173I^2$ MeV). The numbers refer to the bands discussed in detail in the text. The spin and parity of the individual bands are indicated in the following way: $\pi=+, r=+1$, solid line; $\pi=+, r=-1$, short-dashed line; $\pi=-, r=+1$, long-dashed line; $\pi=-1, r=-1$, dotted-dashed line.

1. *Triaxial collective bands below $I=36\hbar$*

This group contains (cf. Fig. 3) the bands 1, 2, 5, 7, 9, and 12. The relevant single-particle diagrams are shown in Figs. 5 and 6. Band 12, originating from the ($\beta_2\simeq 0.28$, $\gamma\geq 20°$) triaxial minimum, develops in spin in a very different way from the bands 1, 2, 5, 7, and 9, the latter corresponding to $\gamma\leq -20°$ equilibrium deforma-

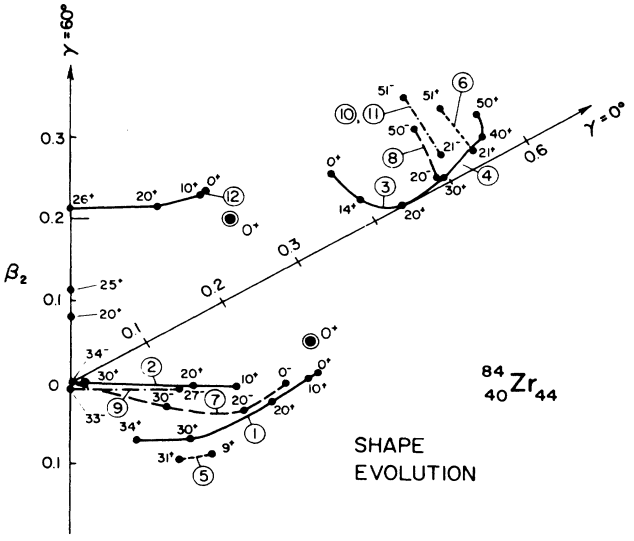

FIG. 4. Shape evolution of the bands represented in Fig. 3. The signature and parity of individual bands are indicated in the same way as in Fig. 3.

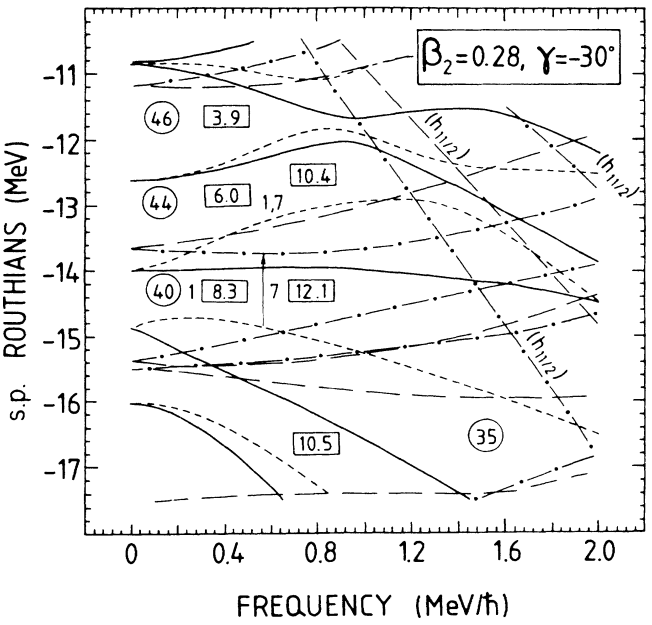

FIG. 5. Neutron single-particle routhians at a deformation $\beta_2=0.28$, $\gamma=-30°$, characteristic of the bands denoted by 1 and 7 in Figs. 3 and 4. The numbers in rectangles refer to the total angular momentum obtained by occupying all the routhians below the position of the rectangle. The position of the middle of a rectangle against the abscissa specifies the relevant rotations frequency. The figure is illustrative of the relevant proton orbitals as well. Orbitals occupied within the rotational bands 1 and 7 are marked by the positions of the respective reference numbers. The spin and parity of the individual levels are indicated in the following way: $\pi=+, r=-i$, solid line; $\pi=+, r=+i$, short-dashed line; $\pi=-, r=-i$, long-dashed line; $\pi=-, r=+i$, dotted-dashed line.

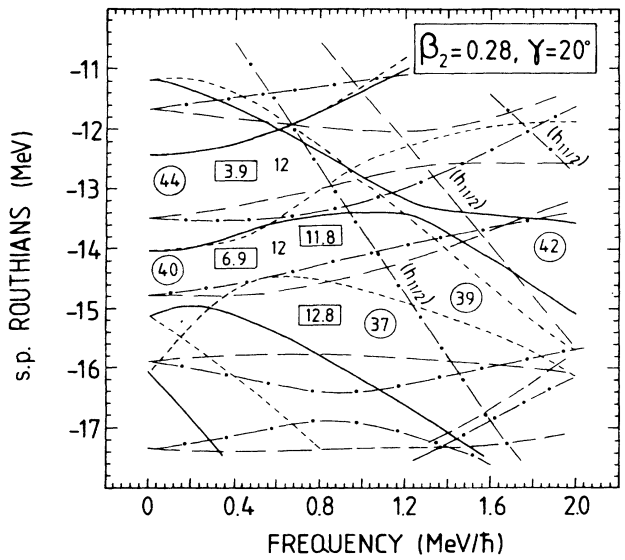

FIG. 6. Similar to Fig. 5, but at a deformation $\beta_2=0.28$, $\gamma=+30°$ typical of band 12 in Figs. 3 and 4.

tions. Although at $I=0\hbar$ both bands 1 and 12 have the same energy (for the symmetry reasons discussed above), band 12 quickly reduces its collectivity and eventually terminates at $\gamma=60°$ ($I=26\hbar$), almost 2 MeV above the yrast band 1; cf. Fig. 3.

Band 7, which has $\pi=-1$ and $N=1$, stays close in deformation to band 1 for $I\leq 22\hbar$. It has the same neutron configuration as band 1; bands 1 and 7 differ in the lowest proton excitation; cf. Fig. 5. Bands 2, 7, and 9 terminate in a spherical shape for $I\geq 30\hbar$. This termination pattern is quite different from the one for band 12 and the one predicted[10] for ^{80}Sr, where the states with a maximum alignment within a band were calculated to have large quadrupole deformations $\beta_2\geq 0.2$ ($\gamma=60°$).

The discussed triaxial bands *do not* contain any aligned $h_{11/2}$ nucleons. The presence of highly aligned particles is typical of the superdeformed bands which become yrast above $I=36\hbar$.

2. *Collective superdeformed bands above $I=30\hbar$*

At the highest spins all the yrast or near yrast bands correspond to strongly elongated shapes with $\beta_2=0.4$–0.6 and $\gamma=0°$–$10°$; see Fig. 4. Bands 3, 4, 6, 8, 10, and 11 belong to this group. As was seen in Figs. 2 and 3, these superdeformed bands develop at spins below $20\hbar$.

The microscopic reason for this can be understood from the single particle diagram, Fig. 7, corresponding to the deformation $\beta_2=0.5$ $\gamma=7°$. The large, 1.5–2 MeV, $N=44$ gap in the single-particle spectrum is clearly seen in the frequency region $0.6\leq\hbar\omega\leq 1.6$ MeV. This unusually large shell opening results in a lowering of the superdeformed bands in the $N=44$ isotones; cf. Ref. 10.

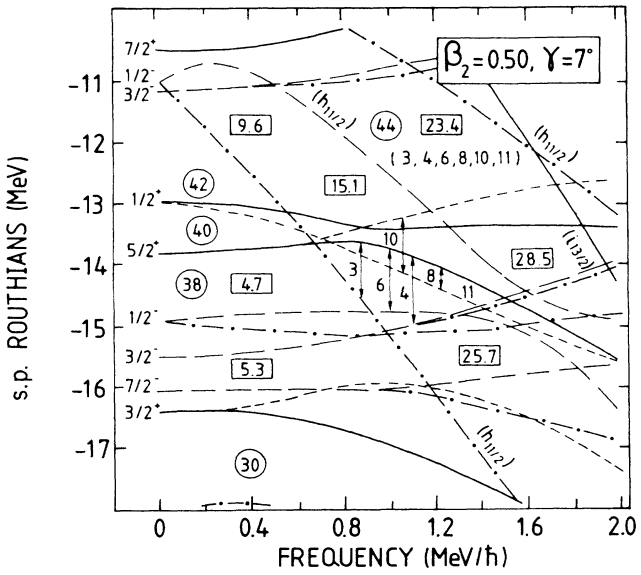

FIG. 7. Similar to Fig. 5, but at a deformation $\beta_2=0.5$, $\gamma=7°$ typical of the superdeformed bands 3, 4, 6, 8, 10, and 11. The levels are labeled with Ω^π quantum numbers, although Ω is not a good quantum number for either $\gamma\neq 0°$ or $\omega\neq 0$.

Due to a "magicity" of the $N=44$ neutron number, all low-lying bands considered in our analysis correspond to a *single* optimal neutron configuration defined by the occupation quantum numbers

$$[N_{\pi=+,r=-i}=11, N_{\pi=+,r=+i}=11\ ,$$
$$N_{\pi=-,r=-i}=11, N_{\pi=-,r=+i}=11]\ .$$

It contains two aligned $h_{11/2}$ neutrons; see Fig. 7.

The superdeformed bands can therefore be distinguished by their proton configurations. The lowest band is the one denoted by 11. Its proton configuration [9, 10, 10, 11] is optimal in the discussed frequency range and corresponds to $\pi=-$ and $r=-1$. The next band, labeled by 8, $(\pi=-, r=+1)$, is built on the proton excitation from the $K^{\pi}=\frac{1}{2}^{+}(r=+i)$ level to the $K^{\pi}=\frac{5}{2}^{+}(r=-i)$ level and therefore its configuration is [10,9,10,11]. Band 6 with $\pi=+$ and $r=-1$ corresponds to the proton excitation from the $\frac{1}{2}^{-}(r=-i)$ level to the $\frac{5}{2}^{+}(r=-i)$ level ([10,10,9,11]). The lowest $(\pi=+, r=+1)$ band labeled by 4, [10,10,10,10], is about 0.8 MeV higher in energy than the optimal band 11. This is due to the large proton excitation energy from the $\frac{3}{2}^{-}(r=+i)$ level to the $\frac{5}{2}^{+}(r=-i)$ level. The $(\pi=-, r=-i)$ band 10 crosses band 11 around $I\simeq 30\hbar$. This can be immediately correlated with the crossing between the $\frac{1}{2}^{+}(r=+i)$ and $\frac{5}{2}^{+}(r=+i)$ orbitals around $\hbar\omega=0.8$ MeV.

All superdeformed configurations discussed so far have *one proton* and *two neutrons* occupying $h_{11/2}$ orbitals. Figure 8 shows alignment plots for these bands. One can notice that they carry about six units of angular momentum alignment relative to the proposed experimental[5] band. The tentative experimental spin-parity assignments do not allow one to analyze in detail the physical reasons for this discrepancy. One can mention, however, that the average dynamical moment of inertia of the discussed superdeformed bands is $J^{(2)}=27\hbar^2/\text{MeV}$, which agrees well with the experimental value $J^{(2)}\simeq 25.5\ \hbar^2/\text{MeV}$.

The band which is closest in alignment to the experimental $(\pi=+, r=+1)$ band is the one labeled 3. Its occupation quantum numbers are identical with those of band 4, but it can easily be separated by means of the excitation quantum number N_{exc} [Eq. (7)]. Microscopically, band 3 is built on the proton excitation from the $h_{11/2,1/2}(r=+i)$ orbital to the $\frac{5}{2}^{+}(r=-i)$ orbital. It contains, therefore, *no* $h_{11/2}$ protons. The alignment of band 4 relatively to band 3 is about $\Delta i=3.5\hbar$ at $E_{\gamma}\simeq 1.8$ MeV, but increases smoothly to the value of $\Delta i\simeq 4.5\hbar$ at $E_{\gamma}\simeq 2$ MeV due to a gradual increase of deformation in band 4 (see Fig. 4). Bands 3 and 4 cross each other around $I=30\hbar$ (or $\hbar\omega=1$ MeV; cf. Fig. 7), but in this spin region they lie about 2.2 MeV above the yrast band 1 (cf. Fig. 3).

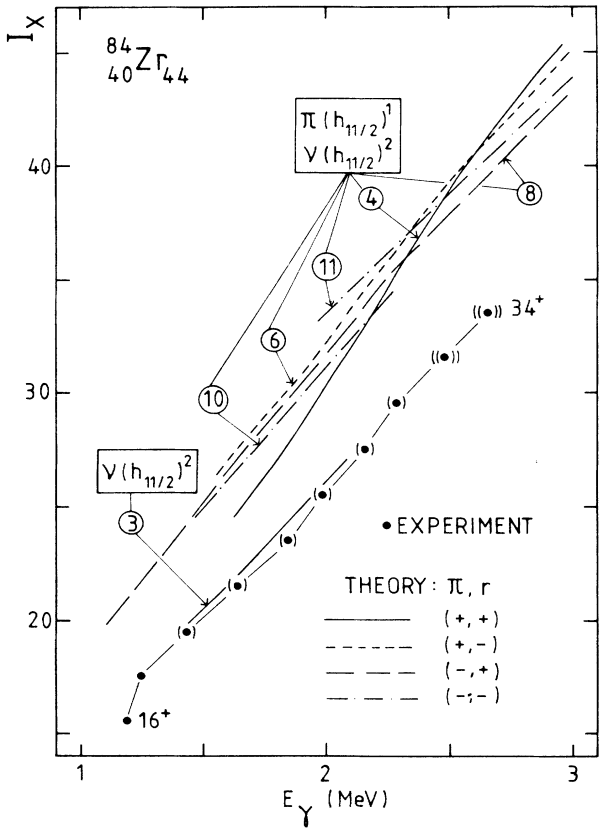

FIG. 8. Angular momentum vs transition energy for the superdeformed bands in ^{84}Zr. Experimental data are taken from Ref. 5.

C. Cranking model analysis of the ^{84}Zr spectrum

The cranking model[30] has been employed to interpret the bands of ^{84}Zr. Figure 9 shows experimental energies in the rotating frame of reference (routhians) versus rotational frequency. The $(\pi=+, r=+1)$ ground band behaves regularly and shows an increase in spin alignment at $0.45 \lesssim \hbar\omega \lesssim 0.6$ MeV (the very-high-spin part of the data for this band is not displayed in Fig. 9). The excited $(\pi,r)=(+,+)$ band, indicated by the symbol T, also gains alignment at $\hbar\omega \gtrsim 0.4$ MeV and approaches yrast at $\hbar\omega\simeq 0.5$ MeV [in fact, the $I^{\pi}=12^{+}$ states in both $(+,+)$ bands are almost degenerate, with energies 5134.5 and 5149.7 keV, respectively]. The negative parity band with $r=-1$, which is lower in energy at low rotational frequencies, crosses the $r=+1$ band at $\hbar\omega=0.66$ MeV.

To get some idea about the structure of these bands, the angular momentum alignment i, the kinematic moments of inertia $J^{(1)}\equiv I_x/\omega$, and the dynamical moments of inertia $J^{(2)}\equiv dI_x/d\omega$ are displayed in Fig. 9.

The $J^{(2)}$ moment of inertia for this yrast $(+,+)$ band exhibits four maxima centered around frequencies $\hbar\omega_1\simeq 0.48$ MeV, $\hbar\omega_2\simeq 0.58$ MeV, $\hbar\omega_5\simeq 0.95$ MeV, and $\hbar\omega_6\simeq 1.1$ MeV. Such "peaks" in the $J^{(2)}$ vs $\hbar\omega$ plot usually indicate band crossings with large interaction strengths $|V|$ or some other structural changes taking place within a rotational band (e.g., changes in deformation or in pairing field). In the $(-,-)$ band two maxima can be seen: at $\hbar\omega_3\simeq 0.45$ MeV and $\hbar\omega_4\simeq 0.63$ MeV. Only one peak can be observed in the $(-,+)$ and excited

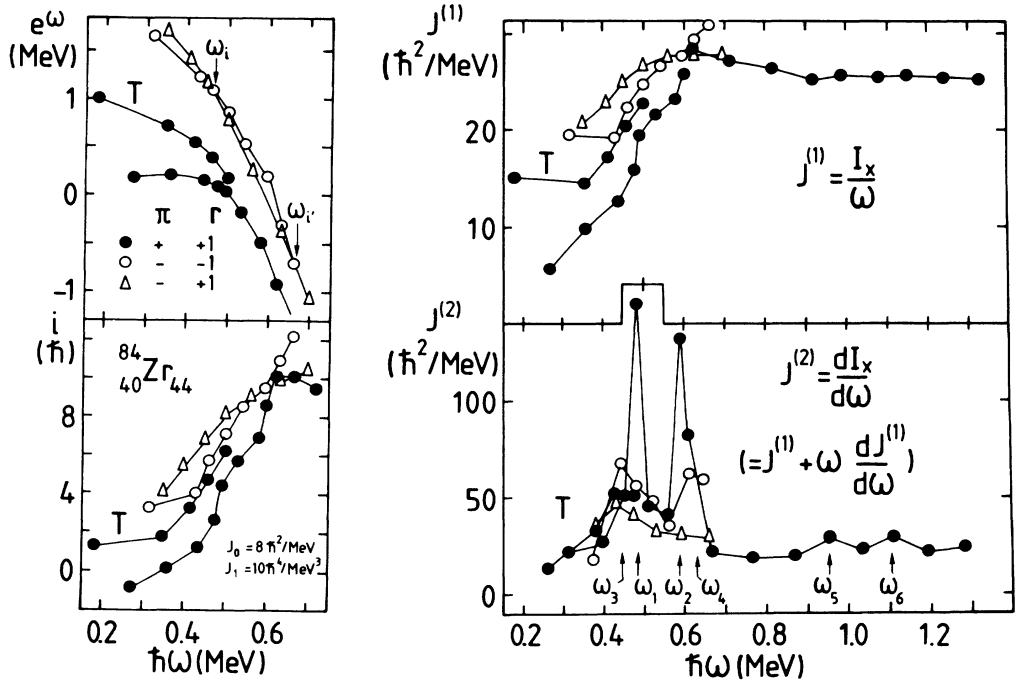

FIG. 9. Cranked shell model analysis of the band structures of ^{84}Zr.

$(+,+)$ bands. At ω_3 for $\hbar\omega > 0.9$ MeV the kinematical moment of inertia of the $(+,+)$ yrast band stays approximately constant, equal to $25\hbar^2$MeV.

In order to interpret the above experimental findings we calculated the quasiparticle routhians for two deformations: $\beta_2=0.28, \gamma=-20°$ [representative of the $(+,+)$ yrast band] and $\beta_2=0.24, \gamma=-35°$ (representative of the negative parity bands after the alignment of the first pair of quasineutrons; see Fig. 4 and discussion below). The results are shown in Fig. 10. The constant pairing gap values, $\Delta_n=\Delta_p=1.4$ MeV, slightly reduced compared with the values at $\omega=0$, were used to account for the weaker pair field at higher rotational frequencies. In order to simplify discussions we employ standard terminology of the cranking shell model (CSM), i.e., the lowest routhians with $(\pi=+, r=-i)$, $(\pi=+, r=+i)$, $(\pi=-, r=-i)$, and $(\pi=-, r=+i)$ are labeled by A, B, E, and F, respectively, while the letter C is reserved for the second $(\pi=+, r=-i)$ orbital [see Fig. 10(a)].

At deformation $\beta_2=0.28$, $\gamma=-20°$, the first $g_{9/2}$ proton crossing is predicted at $\hbar\omega_1\simeq 0.5$ MeV and the first $g_{9/2}$ neutron crossing at $\hbar\omega_2\simeq 0.6$ MeV—in good agreement with the experimental values; see Fig. 9. Also, the calculated gain in alignment, $i_p=5.7\hbar$ and $i_n=5.2\hbar$, agree well with $i_{expt}\simeq(9-10)\hbar$ (cf. Fig. 9). We therefore conclude that two irregularities seen in the $(+,+)$ yrast bands are caused by the alignment of a $g_{9/2}$ proton pair followed by alignment of a $g_{9/2}$ neutron pair.

The lowest negative parity proton excitation corresponds to the two-quasiparticle configuration AE, which has signature $r=-1$. In the neutron system, the signature order of the lowest negative parity orbitals is inverted and the lowest $\pi=-$ excitation (AF) therefore has signature $r=+1$. Experimentally, the $(-,+)$ band is lower in energy up to $\hbar\omega_i\simeq 0.5$ MeV and therefore one can conclude that that band has to correspond to the AF proton configuration [the possibility that the $(-,+)$ band is A_nF_n cannot be excluded, but is unlikely, as both negative parity bands couple at low spins, which, in the latter case, would involve the four-quasiparticle isovector transition].

Calculations without pairing, presented in Fig. 4, show a slight decrease in γ (to about $-35°$) and a slight decrease in β_2 (to about 0.24) in the lowest negative and positive parity bands with angular momentum (the deformation of the $\pi=-$ band is slightly smaller). Calculations including pairing usually reflect the tendency given by the Strutinsky calculations without pairing correlations, but deformation changes are not as gradual and are connected with a shape polarization[31] driving force of aligned quasiparticles. For the position of the Fermi level in the upper half of the $g_{9/2}$ subshell ($N=44$ and also, to a lesser degree, $Z=40$), deformations with large negative γ values ($\gamma\simeq -35°$) and small β_2 are favored.[32] One should therefore expect that:

(i) deformations of the negative parity bands A_pE_p and A_pF_p will generally be smaller compared with the deformation of the g band;

(ii) the alignment of the $g_{9/2}$ neutron pair (A_nB_n) will drive the system toward more negative γ values.

These two observations correspond well to the results presented in Fig. 4.

Diagrams 10(c) and 10(d), calculated at a reduced deformation $\beta_2=0.24$ and $\gamma=-35°$, are representative of the four-quasiparticle $A_pE_pA_nB_n$ and $A_pF_pA_nB_n$ config-

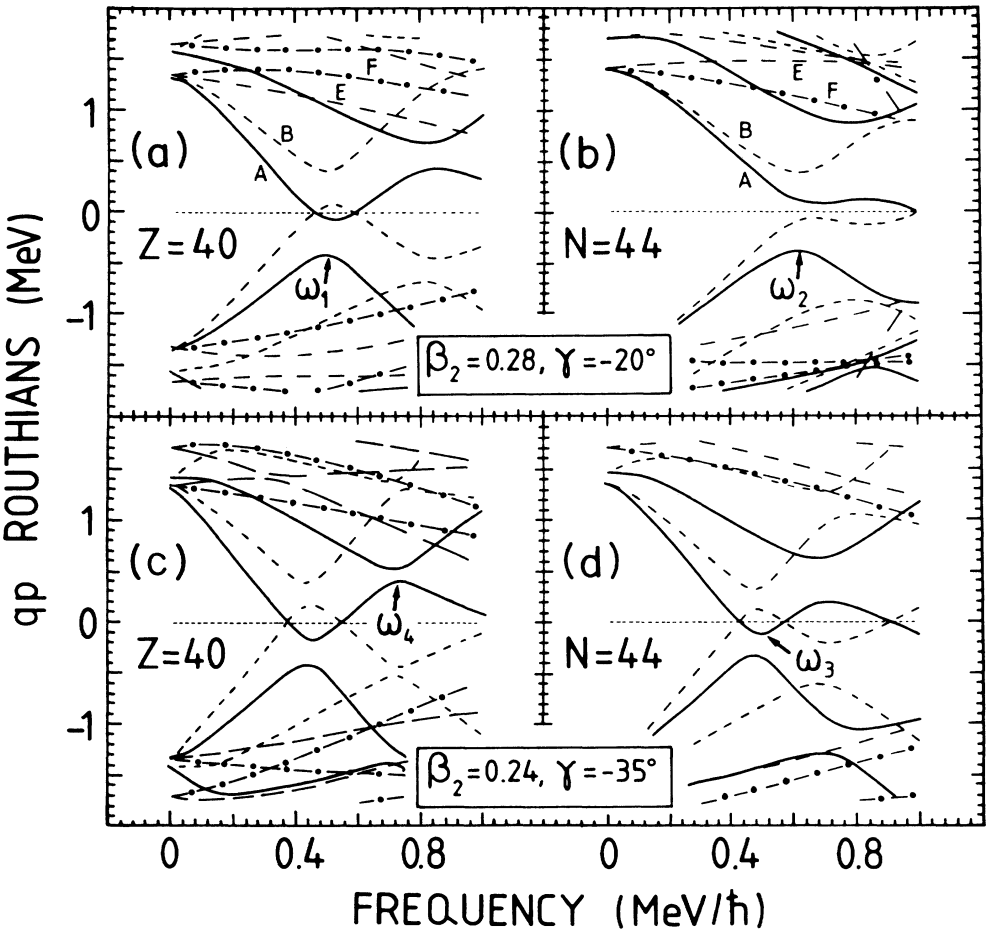

FIG. 10. Proton and neutron quasiparticle routhians in ^{84}Zr. The signature and parity of the individual levels are indicated in the same way as in Fig. 5.

urations. One can immediately see that at this shape the signature order of lowest $\pi=-$ proton excitations is reversed compared with the one from Fig. 10(a), which explains the experimentally observed signature inversion.

The first crossing in negative parity bands, observed at frequency ω_3, cannot be due to the alignment of $g_{9/2}$ quasiprotons (level A_p is blocked), but rather to $g_{9/2}$ quasineutrons. Indeed, calculations reproduce a very reduced value of neutron crossing frequency, $\hbar\omega_c \simeq 0.45$ MeV [see Fig. 10(d)], in the negative parity bands. The second crossing in $\pi=-$ bands, due to the alignment of B_pC_p quasiprotons, is predicted to occur at $\hbar\omega_4 \simeq 0.7$ MeV (slight lowering of $\hbar\omega_4$ due to the reduction of the pairing field after the B_pC_p crossing is also expected). This is the most likely explanation for the second alignment in the $(-,-)$ band. It is not clear, however, why such crossing is not seen in the $(-,+)$, A_pF_p band.

The excited positive parity band T can be interpreted at low spin in terms of a triaxial rotor (see Ref. 5). At higher spins, however, it closely approaches the $\pi=+$ yrast band just before alignment of a $g_{9/2}$ neutron pair (see Fig. 9), which suggests that at $\hbar\omega \geq 0.5$ MeV this band has a dominating A_pB_p component.

The possible explanation for two bumps at ω_5 and ω_6 in the $J^{(2)}$ vs ω curve for the $\pi=+$ yrast band is given in the next subsection, where results of self-consistent-pairing calculations are presented.

D. Self-consistent-pairing calculations

In order to compare the predictions of our model with experiment in a more quantitative way, the HFBC calculations have been performed. Figure 11 presents results of self-consistent-pairing calculations referred to as RBCS (rotating BCS). (Concerning this part of the calculations, we have closely followed the procedure proposed in Ref. 33 and applied in a realistic calculation in Ref. 34.) Here a comparison between the calculated and experimental moments of inertia $J^{(1)}$ (top panel) is given. The calculated pairing gaps are shown in the bottom panel of Fig. 11. For illustration, the results correspond to a fixed deformation $\beta_2=0.28$ and $\gamma=-20°$. Comparison with the results of Fig. 4 shows that this deformation can be considered *representative* for the yrast band up to relatively high ($I \simeq 20\hbar$) spins.

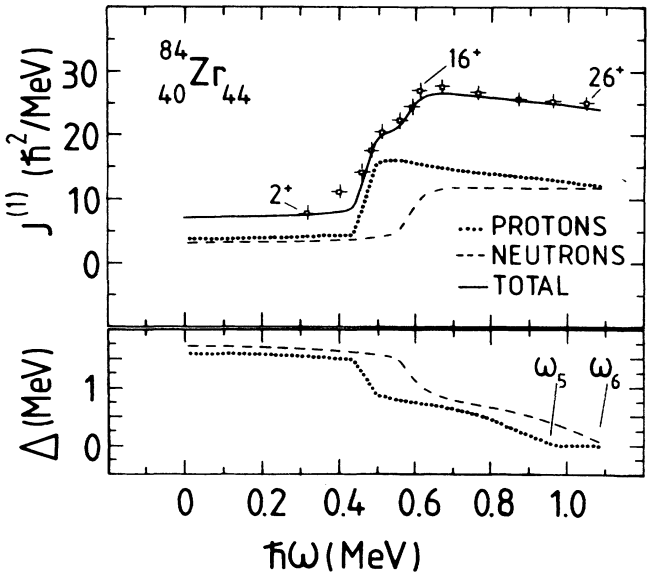

FIG. 11. Results of the self-consistent-pairing calculations (RBCS) for ^{84}Zr. Experimental data are taken from Ref. 5.

The very-low-spin limit, states with $I=(0,2)\hbar$, requires a special comment. Since the calculated absolute minimum at $I=0\hbar$ corresponds to a spherical shape, the nature of the ground state is probably somewhat different from the nature of higher spin states. The most likely process to occur in the low-spin range is change of shape in the yrast states, from $\beta_2\simeq 0$ at $I=0\hbar$ to a moderate deformation at $I=2\hbar$ up to a stabilization at $\beta_2\simeq 0.28$, $\gamma\simeq -20°$ at higher spins. This situation may be further complicated by the presence of a higher lying 2^+ state at 1119 keV and thus by possible interaction between the two $I^\pi=0^+$ and $I^\pi=2^+$ configurations. The fact that the calculated value of the moments of inertia at $I=2\hbar$ agrees with the experiment may be accidental (a quantitative description at such low spin effects goes beyond the scope of the present investigation). Note that the theoretical description of the $J^{(1)}$ moment of inertia for $I\geq 6\hbar$ is quite precise and resembles the experimental results in detail.

At $\hbar\omega=1.1$ MeV the pairing correlations disappear (the Mottelson-Valatin pairing phase transition, Ref. 35. The decrease of the pairing gaps Δ for $\hbar\omega$ above 0.6 MeV is gradual and smooth, and this gives rise to a characteristic nearly linear dependence of $J^{(1)}$ vs ω for $I=16\hbar,18\hbar,\ldots,26\hbar$. In our calculations the BCS pairing phase transitions are predicted to occur at $\hbar\omega_5\simeq 0.96$ MeV and $\hbar\omega_6\simeq 1.1$ MeV for protons and neutrons, respectively. At very similar frequencies two bumps in the experimental $J^{(2)}$ vs ω curve for the $\pi=+$ yrast band are seen in Fig. 9. It has been shown previously[36] that the disappearance of *static* pairing correlations manifests itself in a peak in the dynamical moment of inertia, and experimental evidence for such an effect has been found recently in ^{168}Hf and ^{170}W (see the discussion in Ref. 29). If one excludes possible deformation effects at $\hbar\omega\leq 1.1$ MeV, the proton and neutron Mottelson-Valatin effect is the most plausible explanation of the observed weak irregularities.

It is well known, however, that in the region of a pairing phase transition (or just in the case of weak pairing) the BCS method breaks down. This feature of the BCS method arises because of unconstrained fluctuations in particle number, and in models with good particle numbers pairing correlations are always present to some extent. The possible way to go beyond the BCS method is to account for the pairing fluctuations in a harmonic approximation, i.e., by means of the random-phase-approximation (RPA) approach (see, e.g., Refs. 37 and 38 and references quoted therein) or to perform the particle number projection before variation (see, e.g., Ref. 39 and references quoted therein).

In our paper we have used the latter method in its RFBCS variant, described in detail in Ref. 39. The particle-number-projected energy always lies lower than the BCS energy and does not exhibit artificial fluctuations in the region of very weak pairing. It allows us to compare, with each other, the energies of rotational bands with different seniority calculated at different deformation points. Results of such calculations are presented in Fig. 12, where five theoretical bands are compared with the experimental data from Ref. 5.

Up to spin $I\simeq 26\hbar$ the total energy is fairly well reproduced by the yrast band calculated at $\beta_2=0.28$, $\gamma=-20°$. As in the self-consistent-pairing calculations discussed above, this band contains two aligned $g_{9/2}$ quasineutrons and two aligned $g_{9/2}$ quasiprotons at high spin. From a structural point of view this band resembles the one denoted by 1 in Fig. 3, where, however, the $g_{9/2}$ alignment occurs in a more gradual way. Around $I=28\hbar$ this band is crossed by the superdeformed band 4 ($\beta_2=0.55$, $\gamma=7°$) which, in this region of angular momenta, contains four aligned $h_{11/2}$ quasiparticles (two protons and two neutrons). The lowest superdeformed band of negative parity and signature $r=-1$, denoted as 11 in Fig. 3, lies about 1 MeV above band 4 at $I=36\hbar$ in RFBCS calculations. This is due to stronger pairing correlations in band 4 which lower its energy considerably (cf. Fig. 3). [It is expected (see, e.g., Ref. 38) that pairing correlations above the critical point for the pairing phase transition are strongest in the $\pi=+, r=+1$ bands.] Both bands 4 and 11 have larger moments of inertia and carry more alignment compared with (tentative) experimental data, in quantitative analogy to results presented in Fig. 8. Finally, we present also band 3 with two aligned $h_{11/2}$ quasineutrons calculated at $\beta_2=0.42$, $\gamma=2°$. Its alignment and moment of inertia are very close to the experimental ones above $I\geq 24\hbar$, but it lies far above yrast (cf. also Figs. 3 and 8).

E. Comment on the experimental $B(E2)$ rates

In Ref. 5 lifetimes of the $\pi=+$ yrast band states were measured up to $I^\pi=24^+$, and the transition quadrupole moments

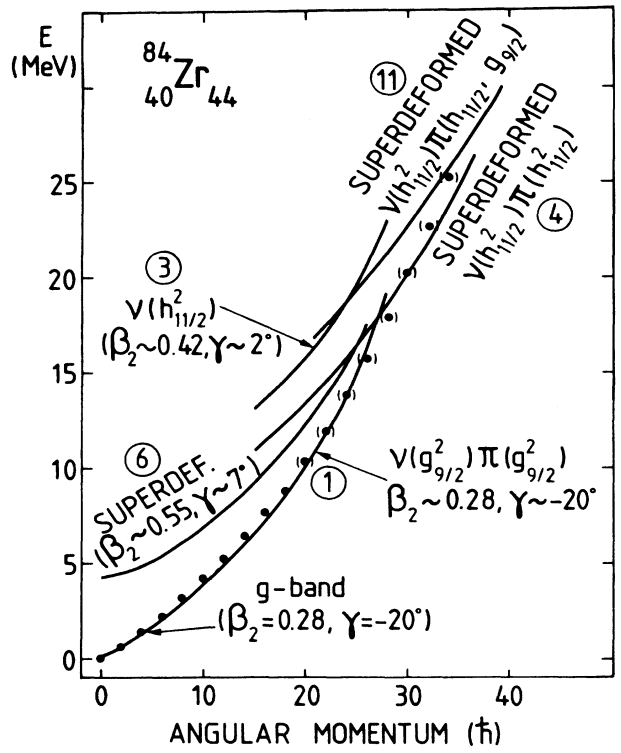

FIG. 12. Total energy calculated using the particle-number-projection (RFBCS) method vs angular momentum for characteristic rotational bands in ^{84}Zr: calculated bands are labeled by means of the aligned quasiparticles and by deformation parameters. The bandhead energies were taken from Strutinsky calculations (with pairing); see Fig. 1.

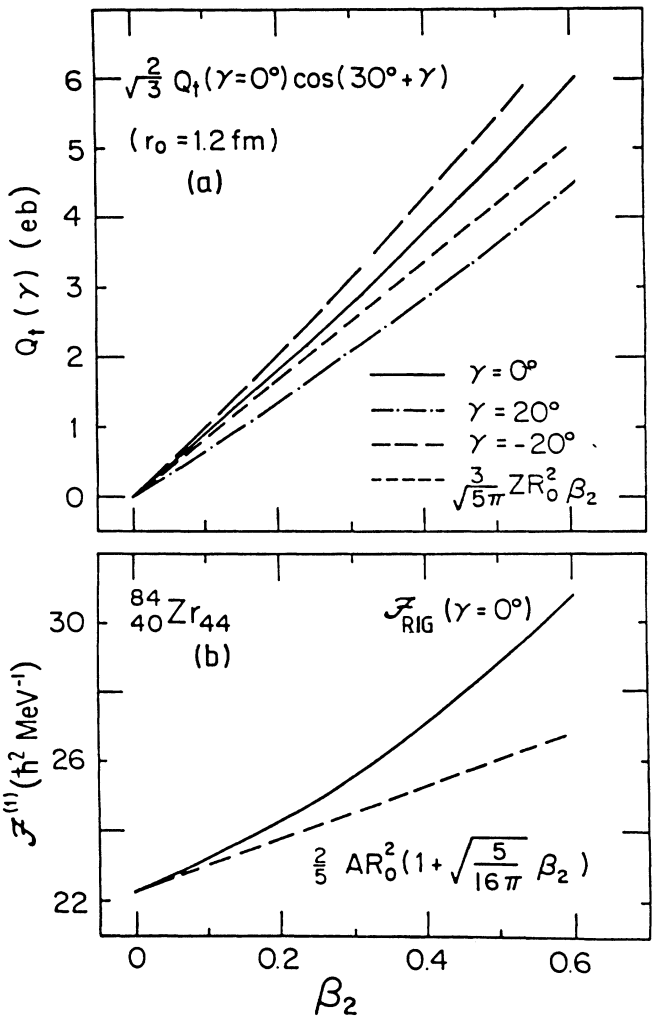

FIG. 13. The rigid-body approximation for the transition quadrupole moment Q_t (top) and moment of inertia (bottom), vs quadrupole deformation β_2.

$$Q_t=\left[\frac{16\pi}{5}B(E2)\right]^{1/2}|\langle I020|I-20\rangle| \tag{11}$$

were determined from these data. The transition quadrupole moments vary from 2 e b at $I^\pi=2^+$ to 1.2–1.5 e b for $I^\pi=6^+-16^+$ and eventually increase to $Q_t\simeq2.5$–4 e b for the $I^\pi=22^+-24^+$ states. Reduced values of Q_t at low and medium spins can be explained in terms of spherical-triaxial shape coexistence for $I=(0-4)\hbar$ and by a strong band mixing in the region of $g_{9/2}$ proton and neutron alignments. Up to $\hbar\omega\simeq0.7$ MeV, where the yrast configuration is probably not disturbed much, one can use the simple, but rather rough, cranking approximation for the Q_t moments (see, e.g., Ref. 40),

$$Q_t\simeq Q_t(\beta_2,\gamma=0°)\cos(30°+\gamma)\frac{2}{\sqrt{3}}\,, \tag{12}$$

to estimate the nuclear deformation.

Figure 12(a) shows the transition quadrupole moments of the uniformly charged liquid drop versus β_2 for three values of γ: $\gamma=-20°$, 0°, and $+20°$. The linear approximation for Q_t at $\gamma=0°[\equiv(3/\sqrt{5\pi})ZR_0^2\beta_2]$ used in Ref. 5 is also shown for comparison. It is immediately seen from Fig. 12 that the deformation $\beta_2\simeq0.3$, $\gamma=-20°$ yields a Q_t value of about 3 e b—which is in satisfactory agreement with experimental data.

Finally, Fig. 13(b) shows the kinematic rigid body moment of inertia, $J^{(1)}$, calculated for axial shapes as a function of β_2. The linear approximation used in Ref. 5 is also shown for comparison. The rigid-body model employed in Ref. 5 neglects the intrinsic (shell) structure of nucleus. One can argue that although such an approximation for Q_t can be justified (multipole moments calculated with a microscopic model depend only on the deformation of an average field; Ref. 40, the calculated moments of inertia are very strongly influenced by shell effects. The term "rigid body moment of inertia" can therefore be applied only to the average value of moments of inertia for a number of near-yrast rotational bands (and under the as-

sumption that pairing correlations are not present in these bands). Therefore the use of the rigid body approximation [see Fig. 13(b)] for only one band cannot be justified.

IV. CONCLUSIONS

The experimental data on ^{84}Zr have been analyzed in terms of the Woods-Saxon cranking model. This approach turns out to give a consistent description of most of the effects observed. Some questions, however, remain open. The main conclusions of this study are as follows:

(i) At very low spins [$I=(0,2,4)\hbar$] the interplay between the *spherical* ground state and well deformed *triaxial* structures is claimed. This shape coexistence leads to a reduction of the transition quadrupole moments at low spins. The lighter zirconium isotopes are expected to be well deformed ($\beta_2\simeq 0.4$) in their ground states.

(ii) Due to the large moment of inertia in the *triaxial* configuration the latter quickly becomes yrast. The two crossings with large interaction seen in the yrast $\pi=+$ band are interpreted in terms of the $g_{9/2}$ proton alignment (at $\hbar\omega\simeq 0.5$ MeV) and the $g_{9/2}$ neutron alignment (at $\hbar\omega\simeq 0.6$ MeV). The reduction of Q_t values at $0.4\leq\hbar\omega\leq 0.6$ MeV can therefore be explained in terms of the configuration mixing in the crossing region.

(iii) Observed negative parity bands are interpreted as two-quasiparticle AE and AF proton configurations. The signature inversion seen in the experimental data at $\hbar\omega\simeq 0.5$ MeV is most likely caused by a change in the nuclear shape. A transition to a more negative γ value and smaller quadrupole deformations also explains the reduction in neutron crossing frequencies in the negative parity bands.

(iv) The excited positive parity band, being interpreted by means of a triaxial rotor model at low spins, probably contains an aligned pair of $g_{9/2}$ quasiprotons at higher angular momenta.

(v) The second alignment observed in the ($\pi=-$, $r=-1$) AE band at $\hbar\omega\simeq 0.64$ MeV is most likely caused by an alignment of the BC quasiproton pair. It is not clear, however, why this crossing is not seen in the AF band.

(vi) The "rigid" character of the rotational spectra after alignment of the second $g_{9/2}$ pair is fully reproduced by the self-consistent-pairing calculations at the $\beta_2\simeq 0.3$, $\gamma\simeq -30°$ shape. Also, the large values of transition quadrupole moments observed for $I^{\pi}=20^+$, 22^+, and 24^+ can be fully accounted for by the above triaxial deformation. Our calculations do not therefore support conclusions drawn in Ref. 5 about the strongly deformed ($\beta_2\simeq 0.43$) axial shape of ^{84}Zr at high spins.

(vii) The pairing phase transitions predicted theoretically at $\hbar\omega_c(\mathrm{p})\simeq 0.97$ MeV and $\hbar\omega_c(\mathrm{n})\simeq 1.1$ MeV correlate well with two irregularities observed in the experimental moment of inertia, $J^{(2)}$, at those frequencies.

(viii) In the spin range above $I=30\hbar$ our calculations show the dominance of very deformed and strongly aligned bands containing at least two aligned $h_{11/2}$ particles. These superdeformed bands already develop at $I\simeq 20\hbar$—due to the large $N=44$ gap in the single-particle routhian spectrum. The calculated alignment in the lowest superdeformed bands is $(5-6)\hbar$ larger than that seen in experimental data.

ACKNOWLEDGMENTS

A significant part of this study was performed during one of the author's (J. D.) stay as a Senior Visiting Fellow to the Daresbury Laboratory; the support from the Science and Engineering Research Council is gratefully acknowledged. One of us (W.N.) acknowledges support from the Danish Science Research Council and the Swedish Science Research Council.

---

*On leave of absence from Institute of Physics, Technical University, Warsaw, Poland.

[1]J. Simpson, M. A. Riley, J. R. Cresswell, P. D. Forsyth, D. Howe, B. M. Nyakó, J. F. Sharpey-Schafer, J. Bacelar, J. D. Garrett, G. B. Hagemann, B. Herskind, and A. Holm, Phys. Rev. Lett. **53**, 648 (1984).

[2]F. S. Stephens, M. A. Deleplanque, R. M. Diamond, A. O. Macchiavelli, and J. E. Draper, Phys. Rev. Lett. **54**, 2584 (1985).

[3]P. J. Twin *et al.* Phys. Rev. Lett. **57**, 811 (1986).

[4]R. B. Piercey, J. H. Hamilton, R. Soundranayagam, A. V. Ramayya, C. F. Maguire, X.-J. Sun, Z. Z. Zhao, R. L. Robinson, H. J. Kim, S. Frauendorf, J. Döring, L. Funke, G. Winter, J. Roth, L. Cleemann, J. Eberth, W. Neumann, J. C. Wells, J. Lin, A. C. Rester, and H. K. Carter, Phys. Rev. Lett. **47**, 1514 (1981).

[5]H. G. Price, C. J. Lister, B. J. Varley, W. Gelletly, and J. W. Olness, Phys. Rev. Lett. **51**, 1842 (1983).

[6]L. Lühmann, M. Debray, K. P. Lieb, W. Nazarewicz, B. Wörmann, J. Eberth, and T. Heck, Phys. Rev. C **31**, 828 (1985).

[7]J. Roth, L. Cleemann, J. Eberth, T. Heck, W. Neumann, M. Nolte, R. B. Piercey, A. V. Ramayya, and J. H. Hamilton, J. Phys. G **10**, L25 (1984).

[8]L. Lühmann, K. P. Lieb, C. J. Lister, B. J. Varley, J. W. Olness, and H. G. Price, Europhys. Lett. **1**, 623 (1986).

[9]R. F. Davie *et al.*, University of Oxford Annual Report, 1984.

[10]W. Nazarewicz, J. Dudek, R. Bengtsson, T. Bengtsson, and I. Ragnarsson, Nucl. Phys. A **435**, 397 (1985).

[11]R. Bengtsson, P. Möller, J. R. Nix, and J.-y. Zhang, Phys. Scr. **29**, 402 (1984).

[12]M. J. A. de Voigt, J. Dudek, and Z. Szymanski, Rev. Mod. Phys. **55**, 9149 (1983).

[13]S. Åberg, Phys. Scri. **25**, 23 (1982).

[14]S. G. Rohozinski, Report of the Institute for Nuclear Research, Warsaw, INR 1520/VII/PH/B, 1972.

[15]J. Dudek, W. Nazarewicz, and T. Werner, Nucl. Phys. **A341**, 253 (1980).

[16]J. Dudek, Z. Szymanski, and T. Werner, Phys. Rev. C **23**, 920 (1981).

[17]G. A. Leander, J. Dudek, W. Nazarewicz, J. R. Nix, and P. Quentin, Phys. Rev. C **30**, 416 (1984).

[18]S. Cwiok, J. Dudek, W. Nazarewicz, J. Skolski, and T. Werner, Comput. Phys. Commun. (to be published).

[19]A. Bohr, Mat.-Fys. Medd. Dansk. Vidensk Selsk. **26**, No. 14 (1952).
[20]V. M. Strutinsky, Nucl. Phys. **A95**, 420 (1967).
[21]R. Bengtsson, S. E. Larsson, G. Leander, P. Möller, S. G. Nilsson, S. Åberg, and Z. Szymanski, Phys. Lett. **57B**, 301 (1975).
[22]C. G. Andersson, S. E. Larsson, G. Leander, P. Möller, S. G. Nilsson, I. Ragnarsson, S. Åberg, R. Bengtsson, J. Dudek, B. Nerlo-Pomorska, and Z. Szymanski, Nucl. Phys. **A268**, 205 (1976).
[23]T. Bengtsson and I. Ragnarsson, Nucl. Phys. **A436**, 14 (1985).
[24]I. Ragnarsson, S. Åberg, H. B. Håkansson, and R. R. Sheline, Nucl. Phys. **A361**, 1 (1981).
[25]P. Ring, R. Beck, and H. J. Mang, Z. Phys. **231**, 10 (1970).
[26]C. J. Lister *et al.*, private communication.
[27]J. Dudek, W. Nazarewicz, Z. Szymanski, and G. A. Leander (unpublished). For a systematic calculation employing the self-consistent Hartree-Fock method, see P. Bonche, H. Flocard, P. H. Heenen, S. J. Krieger, and M. S. Weiss, Nucl. Phys. **A443**, 39 (1985).
[28]C. J. Lister, B. J. Varley, H. G. Price, and J. W. Olness, Phys. Rev. Lett. **49**, 308 (1982).
[29]J. Recht, Y. K. Agarwal, R. P. Blume, M. Guttormsen, H. Hübel, H. Kluge, K. H. Maier, A. Maj, N. Roy, D. J. Decman, J. Dudek, and W. Nazarewicz, Nucl. Phys. **A440**, 366 (1985).
[30]R. Bengtsson and S. Frauendorf, Nucl. Phys. **314**, 27 (1979); **A327**, 139 (1979).
[31]S. Frauendorf and F. R. May, Phys. Lett. **125**, 245 (1983).
[32]R. Bengtsson and W. Nazarewicz, in Proceedings of the XIXth Winter School, Selected Topics in Nuclear Structure, Zakopane, Poland, 1984, edited by Z. Stachura, Jagiellonian University, IFJ Report No. 1268/PL, p. 17.
[33]S. Cwiok, J. Dudek, and Z. Szymanski, Phys. Lett. **76B**, 263 (1978); for more details, also see S. Cwiok, J. Dudek, and Z. Szymanski, Acta Phys. Polon. B **9**, 725 (1978).
[34]S. Cwiok, W. Nazarewicz, J. Dudek, J. Skalski, and Z. Szymanski, Nucl. Phys. **A333**, 139 (1980).
[35]B. R. Mottelson and J. G. Valatin, Phys. Rev. Lett. **5**, 511 (1960).
[36]J. Dudek, W. Nazarewicz, and Z. Szymanski, Phys. Scr. T **5**, 171 (1983).
[37]Z. Szymanski, in Proceedings of the Niels Bohr Centennial Symposium on Nuclear Physics, Copenhagen, 1985, edited by R. A. Broglia, G. B. Hagemann, and B. Herskind (North-Holland, Amsterdam, 1985).
[38]R. A. Broglia and M. Gallardo, in Proceedings of the Second International Conference on Nucleus-Nucleus Collisions, Visby, Sweden [Nucl. Phys. **A447**, 489c (1986)].
[39]W. Nazarewicz, J. Dudek, and Z. Szymanski, Nucl. Phys. **A436**, 139 (1985).
[40]P. Ring, A. Hayashi, K. Hara, H. Emling, and E. Grosse, Phys. Lett. **110B**, 423 (1981).